Journal of Pharmaceutical Analysis 14 (2024) 101024

Contents lists available at ScienceDirect

Journal of Pharmaceutical Analysis

journal homepage: www.elsevier.com/locate/jpa

Original article

Spatial metabolomics reveal metabolic alternations in the injured mice kidneys induced by triclocarban treatment

Peisi Xie [a, 1], Jing Chen [a, 1], Yongjun Xia [b, c], Zian Lin [a], Yu He [a], Zongwei Cai [a, b, *]

[a] Ministry of Education Key Laboratory of Analytical Science for Food Safety and Biology, Fujian Provincial Key Laboratory of Analysis and Detection Technology for Food Safety, College of Chemistry, Fuzhou University, Fuzhou, 350116, China
[b] State Key Laboratory of Environmental and Biological Analysis, Department of Chemistry, Hong Kong Baptist University, Hong Kong SAR, 999077, China
[c] Shanghai Engineering Research Center of Food Microbiology, School of Health Science and Engineering, University of Shanghai for Science and Technology, Shanghai, 200093, China

ARTICLE INFO

Article history:
Received 25 January 2024
Received in revised form
29 May 2024
Accepted 22 June 2024

Handling Editor: Weilong Qu

Keywords:
Triclocarban
Nephrotoxicity
Spatial metabolomics
MALDI mass spectrometry imaging

ABSTRACT

Triclocarban (TCC) is a common antimicrobial agent that has been widely used in medical care. Given the close association between TCC treatment and metabolic disorders, we assessed whether long-term treatment to TCC at a human-relevant concentration could induce nephrotoxicity by disrupting the metabolic levels in a mouse model. Matrix-assisted laser desorption/ionization mass spectrometry imaging (MALDI-MSI) was applied to investigate the alterations in the spatial distributions and abundances of TCC, endogenous and exogenous metabolites in the kidney after TCC treatment. The results showed that TCC treatment induced the changes in the organ weight, organ coefficient and histopathology of the mouse kidney. MSI data revealed that TCC accumulated in all regions of the kidney, while its five metabolites mainly distributed in the cortex regions. The abundances of 79 biomolecules associated with pathways of leukotriene E4 metabolism, biosynthesis and degradation of glycerophospholipids and glycerolipids, ceramide-to-sphingomyelin signaling were significantly altered in the kidney after TCC treatment. These biomolecules showed distinctive distributions in the kidney and displayed a favorable spatial correlation with the pathological damage. This work offers new insights into the related mechanisms of TCC-induced nephrotocicity and exhibits the potential of MALDI-MSI-based spatial metabolomics as a promising approach for the risk assessment of agents in medical care.

1. Introduction

Triclocarban (TCC) is a chemical compound that has gained significance in many fields, such as medical care, due to its antimicrobial properties [1]. It belongs to the class of antibacterial agents known as chlorinated carbanilides and is commonly used as an active ingredient in various products, such as soaps, hand sanitizers, and wound cleansers [2]. It has been found to be particularly effective against gram-positive bacteria, including *Staphylococcus aureus* and Streptococcus pyogenes, which are known to cause various skin infections [3]. Due to its wide application, TCC has been commonly detected in many human body fluids including blood and urine [4–6]. However, instead of its super antiseptic properties, TCC is a typical endorine-disrupting compound that could cause imbalances in human natural hormones and lead to negative effects on reproduction and development [7]. Epidemiological evidences revealed a connection between urinary TCC levels in females and an elevated risk of type 2 diabetes mellitus [8]. Additionally, TCC in umbilical cord blood has been linked to a reduction in gestational age at birth [9], while maternal serum TCC has been associated with fetal anomalies [10]. *In vivo* studies suggested that TCC treatment decreased uterine weight and neonate survival rate in rodents [11,12].

Apart from its endocrine-disrupting abilities, TCC treatment has also been closely associated with many adverse effects on nonreproductive organs [13,14]. For instance, in rodent models, TCC caused a decrease in gut microbiota diversity and a change in microbiota composition [15], as well as promoted colitis and enhanced the development of colon tumors in mice [16]. Zhang et al. [17] reported that in LO2 normal liver cells, TCC induced DNA damage and lipid peroxidation by creating a pro-oxidant cellular

* Corresponding author. State Key Laboratory of Environmental and Biological Analysis, Department of Chemistry, Hong Kong Baptist University, Hong Kong SAR, 999077, China.
E-mail address: zwcai@hkbu.edu.hk (Z. Cai).
Peer review under responsibility of Xi'an Jiaotong University.
[1] Both authors contributed equally to this work.

https://doi.org/10.1016/j.jpha.2024.101024

environment. Administration of TCC to mice fed with a high-fat diet resulted in dyslipidemia and exaggerated the lipid accumulation in the liver [18]. However, to the best of our knowledge, no study has been performed to assess the effects of long-term TCC exposure on the kidney, which is the vital organ responsible for filtering waste products, excess water, and toxins from the blood to produce urine.

Metabolic disorders have been widely utilized to assess health status and predict the risk of chronic diseases in healthcare [19,20]. Metabolomics analysis is able to offer comprehensive and dynamic metabolic responses and variations of living system to toxic stimuli [21,22]. This makes it particularly valuable in identifying new toxic biomarkers and unraveling the underlying toxic mechanisms. Many previous works used the liquid chromatography-mass spectrometry-based (LC-MS-based) metabolomics to investigate the toxic mechanisms of TCC. Li et al. [18] found that TCC led to metabolic disorders in mice liver by inhibiting the glucose oxidation, promoting the gluconeogensis and tricarboxylic acid cycle, and enhancing the β-oxidation of fatty acids. Zhang et al. [15] reported that TCC disrupted the liver homeostasis through causing the oxidative damage and promoting the glycolysis and single-carbon metabolism. Xie et al. [23] demonstrated that TCC induced metabolic alterations in mice heart by inhibiting the β-oxidation, fatty acid synthesis and tricarboxylic acid cycle. These works offer abundant insights into the disruption of diverse metabolic pathways in targeted organs, enhancing our comprehension of the toxic impacts of TCC. However, limited knowledge exists regarding the spatial distributions of metabolites within these organs, which is crucial for revealing the intricate pathological mechanisms associated with TCC-induced organ injuries.

Matrix-assisted laser desorption/ionization mass spectrometry imaging (MALDI-MSI) is an innovative imaging technique that does not require labeling and is highly sensitive for detecting various metabolites [24–26]. It is considered one of the most suitable tools for spatial metabolomics due to its capability to simultaneously provide both molecular and spatial information. In clinical research, increasing studies have applied spatial metabolomics to explore the toxic mechanisms of various drugs [27,28]. Wang et al. [29] found levels of 38 metabolites were altered in rat kidneys after the administration of a known nephrotoxic drug (aristolochic acid). These metabolites in kidneys showed a favorable spatial correspondence with the histopathological abnormalities. Chen et al. [30] investigated the metabolic responses in lung cancer cell spheroids after treatment with an anticancer drug (hydroxychloroquine). They discovered that this drug induced the alterations of the spatial composition of various biomolecules in the proliferative and necrotic regions of cell spheroids. However, no studies have applied spatial metabolomics to investigate the related toxic mechanisms of TCC in different organisms.

Hence, in order to assess the potential impacts of TCC on human kidneys, we chose the mice as the animal model due to their genetic, biological, and anatomical characteristics that closely mimic those of humans [31]. Besides, the similarity in the nephron structure and function between the mice and humans facilitates the study of drug effects on renal health and disease progression [31,32]. The long-term TCC-treated mice model combined with histopathological examinations was used to assess the effects of TCC treatment on mice kidneys at a human-relevant concentration. The spatial distributions of TCC and its five metabolites in kidneys were investigated by MALDI-MSI. Besides, a comparative MSI analysis of endogenous metabolites in kidneys between the TCC-treated and control groups was performed to screen potential biomarkers and related pathways. Our work may offer a novel perspective on the mechanisms of TCC-induced nephrotoxicity in mice.

2. Materials and methods

2.1. Chemicals and reagents

Methanol (MeOH), hydrochloric acid (HCl), dichloromethane (DCM), and ethanol (EtOH) were purchased from Merck (Darmstadt, Hesse, Germany). 2,5-dihydroxybenzoic acid (DHB), dimethyl sulfoxide (DMSO), *Trans*-2-[3-(4-*tert*-butylphenyl)-2-methyl-2-propenylidene]malononitrile (DCTB), hematoxylin and eosin (H&E), and 1,5-diaminonaphthalene (1,5-DAN) were purchased from Sigma-Aldrich (St. Louis, MO, U.S.A.). TCC was purchased from Santa Cruz Biotechnology (Dallas, TX, U.S.A.). Sesame oil was purchased from Yihai Kerry Arawana Holdings Co., Ltd. (Shanghai, China). The Agilent tuning mix was purchased from Agilent Technologies (Santa Clara, CA, U.S.A.).

2.2. Animal experiments

Three-week old female BALB/c mice were purchased from the Laboratory Animal Center of Charles River (Beijing, China). All the animal experiments were in accordance with the guidelines approved by the Institutional Animal Care and Use Committee of Fuzhou University (Approval number: KS2023-SG-020). TCC was dissolved in DMSO and diluted with sesame oil. TCC in oil was administered once daily to the mice with a dosage of 0 (control group) or 1 mg/kg/day (TCC group). Each group contained 13 mice. The dosage of 1 mg/kg/day was comparable to those detected in the human body. According to the TCC (588 μg/L) determined in the human urine [33], 27% of TCC excreted by the urine [34], and the average daily urine output (1.4 L) [35], an adult can be exposed to TCC at a level as high as 3 mg/kg/day [36,37]. Besides, previous works demonstrated that for a woman consuming 32.95 g of shower gels and bar/liquid soap daily containing 1.5% TCC, she could be exposed to TCC at a level about 10 mg/kg/day [15]. After 142 days of continuous TCC treatment, all mice were euthanized to collect the kidneys. The organ coefficient of the kidney was calculated using the following formula: organ coefficient of the kidney = (weight of the kidney/total body weight) × 100%. All samples were immediately stored at −80 °C until further experiments.

2.3. Histological staining

The kidneys were sliced by using a CryoStar NX70 cryostat (Thermo Fisher, Waltham, MA, U.S.A.) at a thickness of 10 μm and stained with H&E to facilitate the identification of histopathological lesions. The staining procedure was described as follows: rinsing with water (2 s); immersing in hematoxylin (3 min); washing with flowing water (1 min); dipping in EtOH containing 1% HCl (2 s); washing with flowing water (3 min); immersing in eosin (6 s); washing with flowing water (3 min). Stained tissue sections were examined using a BDS400-FL inverted microscope (Chongqing Optic Instrument Co., Ltd., Chongqing, China) at a magnification of 20×.

2.4. Sample preparation for MALDI-MSI

Mice kidneys were placed on a cutting stage for stabilization. Samples were sliced by using the CryoStar NX70 cryostat at a thickness of 10 μm and mounted onto indium tin oxide slides. These slides were dehydrated in a vacuum desiccator for 1 h before the matrix deposition. Three matrices, including the DHB matrix (20 mg/mL in 70% MeOH), DCTB matrix (6 mg/mL in 30% DCM and 70% MeOH), and 1,5-DAN matrix (6 mg/mL in 70% MeOH), were prepared in glass jars. These matrices were sprayed on ITO slides by using the HTX H5 sprayer (HTX Technologies, Chapel Hill, NC, U.S.A.). The instrumental parameters employed were as follows: a flow rate

of 0.03 mL/min; a velocity of 2,000 mm/min; a tracking spacing of 2 mm; a pressure of 10 psi; a total of 16 spray cycles; a drying time of 20 s for the 1,5-DAN and DHB matrices, and 10 s for the DCTB matrix. The temperature of the spray head was set at 66 °C for the 1,5-DAN and DHB matrices, and 50 °C for the DCTB matrix.

2.5. Data acquisition and analysis of MALDI-MSI

The timsTOF fleX MALDI-2 instrument (Bruker Daltonics, Bremen, Germany) was utilized for MSI experiments in the reflection mode and calibrated by using the Agilent tuning mix. The quadrupole-time-of-flight mass analyzer of this instrument has a resolving power of 50,000. MALDI-MS spectra were collected in both negative and positive ionization modes, covering a mass range of *m/z* 50 to 1050, with a laser operating frequency of 10,000 Hz, a laser power of 90%, and the laser shots of 300 per pixel. A laser size of 50 μm in the M5 small mode was used to generate MALDI images. For metabolite ions with *m/z* < 400, the following main optimized instrumental parameters were used: funnel 1 radio frequency (RF) (200 voltage peak-peak (Vpp)), transfer time (60 μs), multipole RF (200 Vpp), pre pulse storage (6 μs), funnel 2 RF (200 Vpp), collision RF (600 Vpp). For metabolite ions with *m/z* > 400, the following main optimized instrumental parameters were used: funnel 1 RF (500 Vpp), transfer time (110 μs), multipole RF (1000 Vpp), pre pulse storage (10 μs), funnel 2 RF (500 Vpp), collision RF (1200 Vpp).

All MSI raw data were imported to the software of SCiLS Lab MVS Version 2024a premium 3D for performing all MSI analyses. Methods of weak denoising and total ion count were utilized for processing ion images and normalizing MALDI spectra, respectively. The segmentation analysis was performed by using the clustering algorithms (bisecting k-means and correlation distance) and the methods (weak denoising and total ion count) to distinguish different internal structures of the mice kidney sections. The probabilistic latent semantic analysis (pLSA) was conducted to distinguish differences in metabolism among different regions in kidneys between control and TCC groups. The differential statistical analysis of average intensities of endogenous metabolites in ten tissue sections from five mice kidneys per group was carried out using the paired *t*-test. The tentative assignment of all metabolites was carried out by searching two public databases, Human Metabolome Database and LIPID MAPS, with a criterion of mass accuracy < 5 ppm. Metabolites that showed significant changes were selected based on the criterion of a fold change < 0.8 or > 1.2 and a *p* value < 0.05. Some of these metabolites with relatively high signal intensities were identified by MALDI-tandem mass spectrometry (MALDI-MS/MS) (Fig. S1).

3. Results and discussion

3.1. Segmentation analysis of the frozen kidney sections

The use of rodent models (e.g., mice) in biomedical research is predicated on the significant physiological and anatomical similarities that are shared with humans [38]. Both the human and mouse kidneys possess comparable structural features, including the presence of nephrons as the functional units responsible for the filtration, re-absorption, secretion, and excretion processes [31]. The nephron organization within the cortex and medulla and the regulation of various functions by hormonal and neuronal signals follow parallel patterns in both species [31,32]. These fundamental similarities provide a strong rationale for the use of mice models to predict potential impacts of pharmacological agents (e.g., TCC) on human kidneys.

Previous works demonstrated that similar to humans, the internal structure of the mouse kidney consists of four main regions including the outer cortex, inner cortex, medulla, and renal pelvis [32]. In order to investigate the metabolic alterations in different regions of the kidneys treated with TCC, we firstly performed the segmentation analysis of the frozen sections of the mice kidneys. As shown in Figs. 1A and B, four regions including the yellow outer cortex, green inner cortex, purple medulla, and orange renal pelvis, were found in kidney sections. There were distinct divisions among these four regions from the results of the plots of pLSA (Fig. S2A), suggesting notable variations in cell metabolism among different regions. In the loading plot, several ions, such as ions at *m/z* 718.5363, 772.5263, 865.5852, and 905.6526, were observed outside the 95% confidence ellipse (Fig. S2B). These ions acted major roles in differentiating these four structures in kidneys. As depicted in Figs. 1C–F, $[PE(34:0)-H]^-$ at *m/z* 718.5363 mainly located in the outer cortex; $[PE(O-40:8)-H]^-$ at *m/z* 772.5263 predominantly distributed in the inner cortex; $[PI(36:0)-H]^-$ at *m/z* 865.5852 mainly located in the medulla; PI(O-40:1) at *m/z* 905.6526 predominantly distributed in the renal pelvis.

3.2. Evaluation of kidney injuries in mice treated with TCC

In order to test the effects of long-term TCC treatment on kidneys, mice were treated with TCC at a human-relevant concentration (1 mg/kg/day) for 142 days. As shown in Figs. 2A–C, TCC treatment did not affect the body weight but significantly reduced the weight and organ coefficient of the kidney in mice. Further histological analysis (Fig. 2D) by using the H&E staining revealed that after TCC treatment, extensive infiltration of inflammatory cells was observed in the renal glomerulus of the cortex. In the medulla, compared to the control group, a disordered arrangement of renal tubular epithelial cells was found. In the TCC-treated pelvis, tubulointerstitial expansion and thinning were found. Our results were somewhat similar to those reported in some previous studies, demonstrating that TCC treatment at human-relevant concentrations (1 mg/kg/day or 50 μg/kg/day) led to pathological changes in some non-reproductive tissues in rodents, such as the inflammation in the colon and the accumulation of lipid droplet in the liver [16,37].

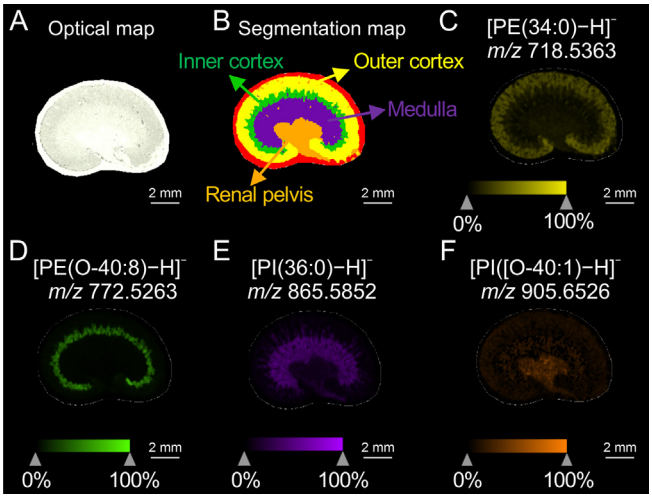

Fig. 1. Segmentation analysis of a frozen kidney section. (A) Optical map and (B) segmentation map of one kidney section. (C–F) Representative images of four ions including [phosphatidylethanolamine(34:0)−H]⁻ ([PE(34:0)−H]⁻)) (C), [phosphatidylethanolamine(O-40:8)−H]⁻ ([PE(O-40:8)−H]⁻)) (D), [phosphatidylinositol(36:0)−H]⁻ ([PI(36:0)−H]⁻)) (E), and [phosphatidylinositol(O-40:1)−H]⁻ ([PI(O-40:1)−H]⁻)) (F) distributing in four regions of the kidney section. All scale bars were 2 mm.

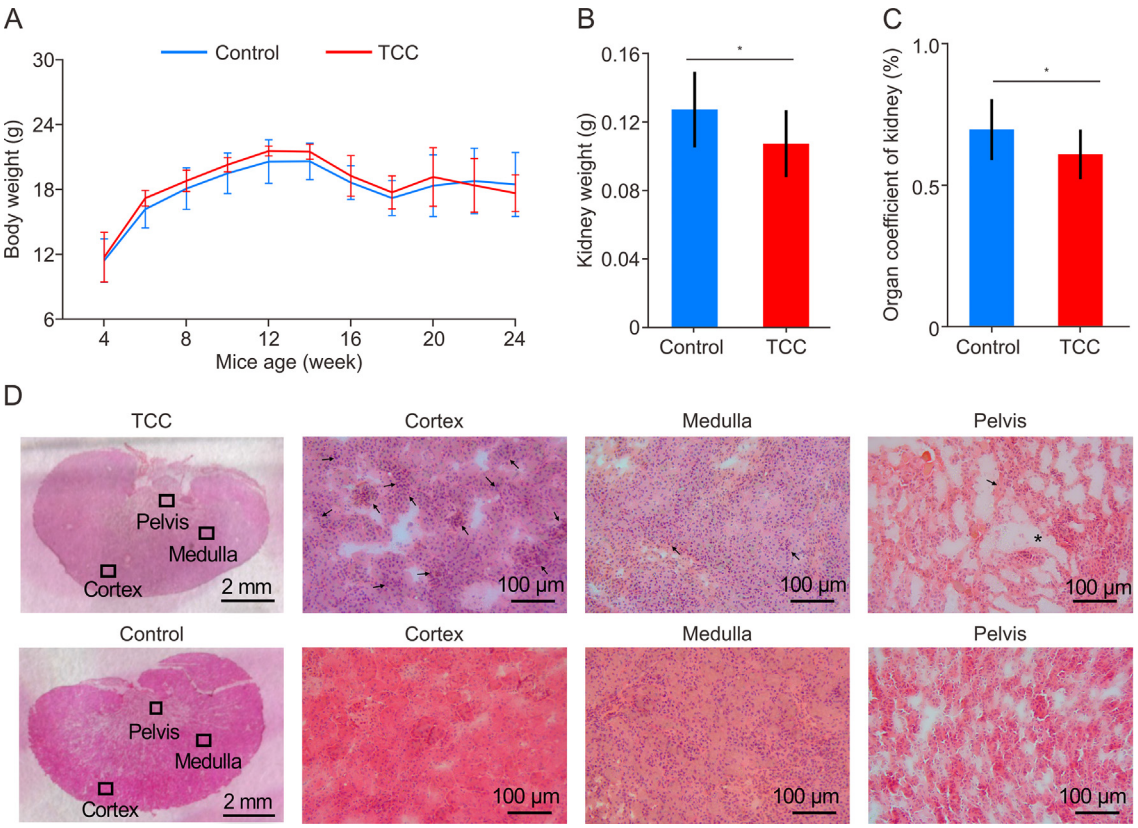

Fig. 2. Evaluation of kidney injuries in mice treated with triclocarban (TCC). (A) Body weight changes. (B) Kidney weight. (C) Organ coefficient of the kidney. (D) Hematoxylin and eosin (H&E) staining of kidney sections between control and TCC groups. Prominent morphological changes were indicated by black asterisks and arrows. The magnified regions in the cortex, medulla, and pelvis of kidney sections at 20× magnification were represented by black boxes. Data are shown as mean ± standard deviation (SD). Each group contained 13 mice. ($^{*}P < 0.05$).

3.3. Distributions of TCC and its metabolites in kidneys

Previous works demonstrated that after TCC treatment, a total of 18 exogenous metabolites were detected in the mice liver by using the LC-MS/MS [15]. In the mice liver, TCC and its metabolites could undergo reactions of dechlorination (e.g., hydroxy-3,4-dichlorocarbanilide (DHC)), hydroxylation (e.g., hydroxy-TCC (OH-TCC) and dihydroxy-TCC (diOH-TCC)), glucuronide/sulfate conjugation (e.g., TCC-glucuronide (TCC-G), OH-TCC-sulfate (OH-TCC-S), OH-TCC-G, DHC-S, DHC-G, and diOH-TCC-G), methylation (e.g., methoxy-TCC-G (MeO-TCC-G)), and glutathione (GSH) conjugation (e.g., DHC-GSH) [15]. In order to investigate the biotransformation of TCC in mice kidneys, we compared the obtained *m/z* values from MALDI spectra in the kidneys between control and TCC groups. We selected the DCTB as the MALDI matrix because our previous works demonstrated that the DCTB matrix showed excellent signal responses for detecting chlorinated carbanilides in negative ionization mode [39,40]. The results showed that a total of 12 ions were detected in the kidney sections in the TCC group but not in the control group. These ions were further assigned to $[TCC-H]^-$ at *m/z* 312.9708 and 314.9679, $[OH-TCC-H]^-$ at *m/z* 328.9657 and 330.9628, $[OH-TCC-S-H]^-$ at *m/z* 408.9225 and 410.9197, $[DHC-H]^-$ at *m/z* 295.0047 and 297.0019, $[OH-TCC-G-H]^-$ at *m/z* 504.9978 and 506.9951, and $[DHC-S-H]^-$ at *m/z* 374.9612 and 376.9587 (Figs. 3 and S3). The presence of two dominant ion peaks for each compound ion was due to chlorine's two major isotopic peaks that are chlorine-35 and chlorine-37.

Previous studies showed that hydroxylation was found to be the primary pathway for TCC phase I metabolism in the kidneys of mice, which led to the formation of OH-TCC as the main monohydroxylated specie [7,15]. Besides, the formation of the dechlorinated hydroxylated metabolite (e.g., DHC) was also identified in both *in vitro* and *in vivo* studies [41,42]. In mammalian tissues, OH-TCC and DHC would further undergo phase II metabolism, leading to the formation of OH-TCC-S, OH-TCC-G, and DHC-S (Fig. 3). As shown in Figs. 3 and S3, after TCC treatment for 142 days, TCC accumulated in all regions of the kidney section, while its five metabolites were mainly distributed in the inner cortex. Notably, aside from the inner cortex region, the outer cortex also exhibited high intensities of these five metabolites, followed by the renal pelvis where low intensities of these metabolites were also observed (Figs. 3 and S3).

Previous works demonstrated that phase I metabolism involves the introduction of functional groups, such as the hydroxyl group, into the parent compound through the oxidation reaction [43,44]. This process can result in the formation of reactive intermediates or metabolites that have the potential to be toxic to cells and tissues of living systems. Phase II metabolism involves the conjugation of the parent compound or its phase I metabolites with endogenous molecules, such as glucuronic acid and sulfate [45]. This conjugation process generally leads to the formation of more water-soluble and less toxic metabolites that can be easily eliminated from the body. In our study, two phase I metabolites (OH-TCC and DHC) predominantly distributed in the cortex regions (Fig. 3), suggesting that TCC treatment may induce cellular damages in these regions. This was proven by the results of the pathological analysis, demonstrating a severe inflammatory cell infiltration in the cortex. Besides, TCC, an antimicrobial ingredient, also exhibits a potent

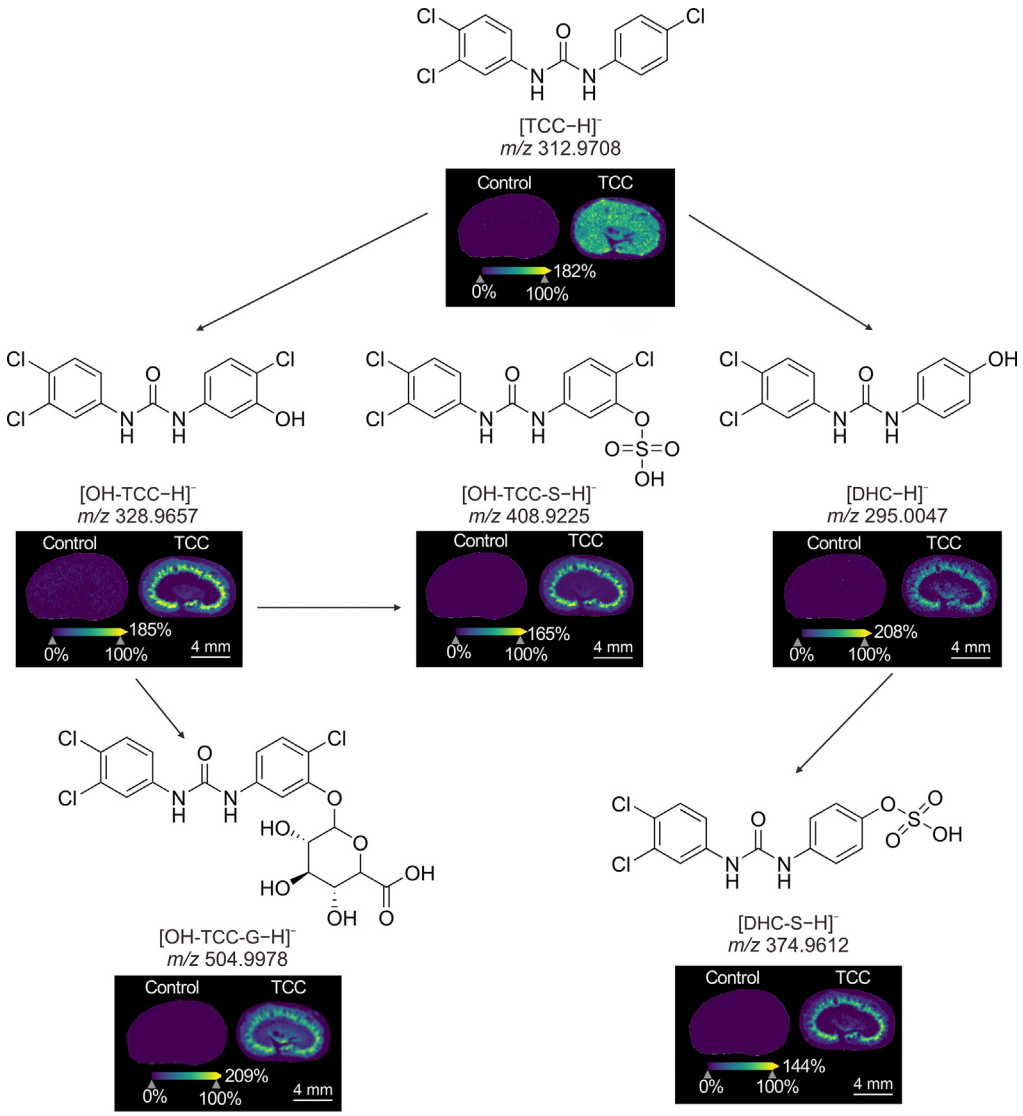

Fig. 3. Spatial distributions of triclocarban (TCC) and its five metabolites in kidney sections between control and TCC groups.

inhibition of the human soluble epoxide hydrolase (a key enzyme associated with the regulation of blood pressure, inflammation, and pain) and causes oxidative stress in living organisms [46–48]. The accumulated TCC in the full region of the kidney (Fig. 3) may also contribute to the morphological alterations in various regions of the kidney (Fig. 2D).

3.4. TCC treatment disturbed the lipid metabolism in mice kidneys

Lipids are a category of metabolites that are vital in numerous cellular processes, including energy storage, signal transmission, survival, and apoptosis [39,40]. Many studies showed that irregular changes in metabolic levels were strongly associated with TCC treatment [15,17,37]. To investigate the *in situ* changes of endogenous lipids within the kidneys treated with TCC, we performed MALDI-MSI-based spatial metabolomics in the kidneys between control and TCC groups. DHB and 1.5-DAN were used as the MALDI matrices in positive and negative ionization modes, respectively. In positive ionization mode, a total of 91 lipids including 8 diacylglycerols, 2 lysophosphatidylglycerols (LPGs), 6 lysophosphatidylcholines (LPCs), 3 lysophosphatidylserines (LPSs), 7 phosphatidylglycerols (PGs), 10 phosphatidylethanolamines (PEs), 27 phosphatidylcholines (PCs), 8 phosphatidylserines (PSs), 7 triglycerides (TGs), and 13 sphingomyelins (SMs) were detected (Table S1). In negative ionization mode, a total of 125 lipids including 15 fatty acids (FAs), 1 LPG, 2 LPSs, 7 lysophosphatidic acids (LPAs), 3 lysophosphatidylinositols (LPIs), 10 lysophosphatidylethanolamines (LPEs), 9 PGs, 24 PEs, 9 PSs, 15 phosphatidylinositols (PIs), 24 phosphatidic acids (PAs), 2 ceramides (Cers), and 4 ceramide-1-phosphates (CerPs) were detected in kidney sections (Table S2).

The results of pLSA score plots suggested that there were separations in four regions of kidney sections in negative and positive modes between control and TCC groups (Fig. 4A). Among all the detected lipids, intensities of 69 lipids including 4 FAs, 1 TG, 2 Cers, 2 CerPs, 7 SMs, 1 LPS, 1 LPI, 1 LPE, 7 PAs, 16 PEs, 3 PGs, 19 PCs, 3 PIs, and 2 PSs were significantly changed in the sections of kidneys treated with TCC (Table S2). These lipids were involved in two pathways including the Cer-SM signaling and the biosynthesis and degradation of glycerophospholipids (GPs) and glycerolipids (GLs) (Fig. 4B). All significantly changed lipid species in FA, TG, LPI, LPE, PA, PE, PG, PC, and PI in TCC-treated kidneys had reduced intensities, while all significantly changed lipid species in LPS, SM,

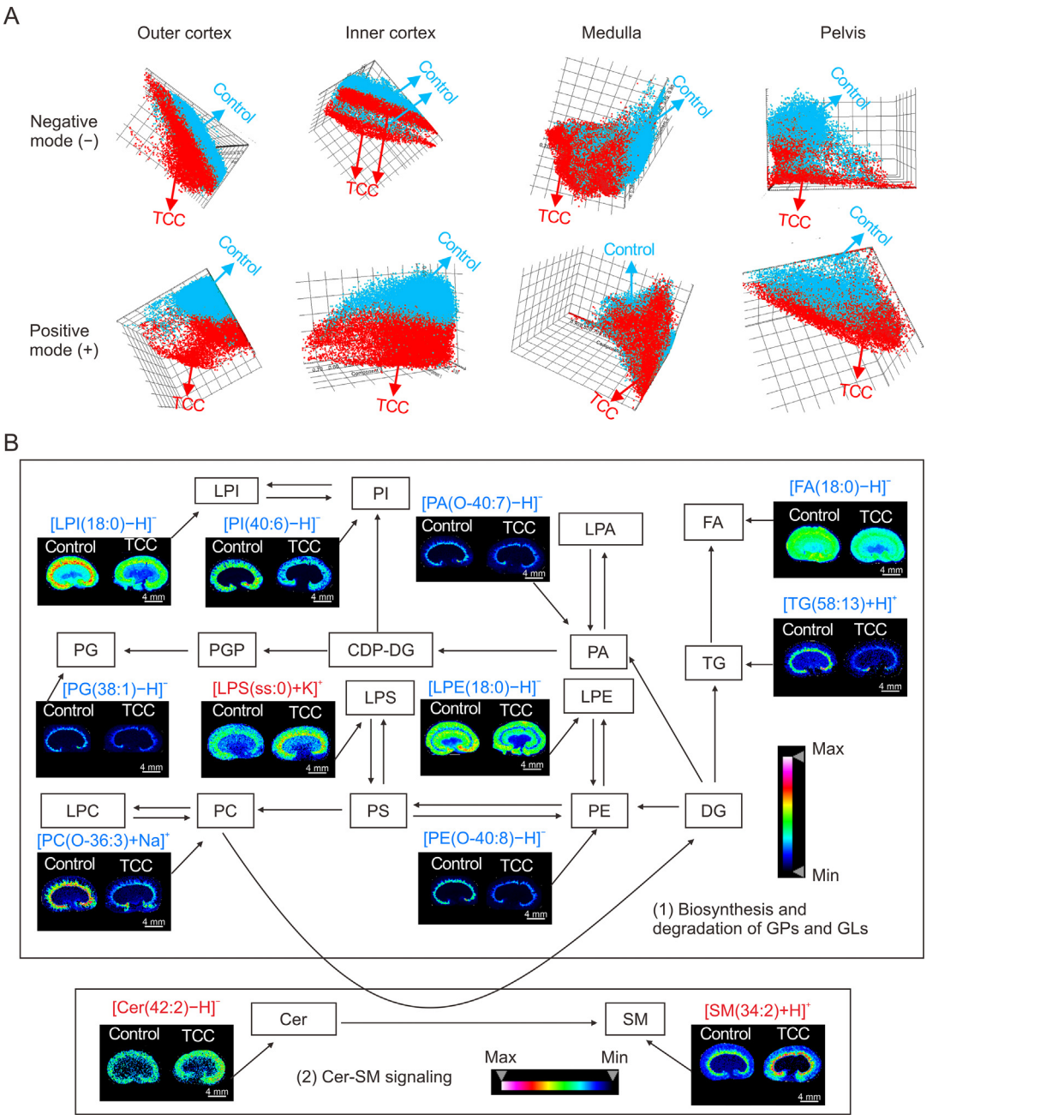

Fig. 4. Matrix-assisted laser desorption/ionization mass spectrometry imaging (MALDI-MSI) analysis of lipids in mice kidney sections. (A) The probabilistic latent semantic analysis (pLSA) score plots based on matrix-assisted laser desorption/ionization (MALDI) profiles of four regions in kidney sections in negative and positive ionization modes ($n = 10$). (B) Ion images of metabolites involved in lipid metabolism in kidney sections between control and triclocarban (TCC) groups. The upregulated and downregulated lipids in kidney sections were represented by the red and blue colors, respectively. LPI: lysophosphatidylinositol; PI: phosphatidylinositol; PG: phosphatidylglycerol; CDP: cytidine diphosphate; LPS: lysophosphatidylserine; LPE: lysophosphatidylethanolamine; PS: phosphatidylserine; PC: phosphatidylcholine; LPC: lysophosphatidylcholine; LPA: lysophosphatidic acid; PA: phosphatidic acids; PE: phosphatidylethanolamine; FA: fatty acid; PGP: phosphatidylglycerol phosphate; DG: diacylglycerol; TG: triglyceride; Cer: ceramide; SM: sphingomyelin.

and Cer in TCC-treated kidneys had increased intensities (Tables S1 and S2). For two significantly changed lipid species in PS, PS(32:0) had increased intensities in TCC-treated kidneys, while PS(O-40:6) had reduced intensities in TCC-treated kidneys (Fig. S3 and Table S1). A majority of these significantly changed lipid species, such as PI(40:6), PA(O-40:7), TG(58:13), PG(38:1), LPS(22:0), PC(O-36:3), PE(O-40:8), Cer(42:2), and SM(34:2), had changed levels in the cortex regions (Fig. 4B; Tables S1 and S2). Some lipid species, such as LPI(18:0) and FA(18:0), had changed levels in all regions (Fig. 4B; Tables S1 and S2).

TG and FA play crucial roles in cellular energy storage and metabolism [49]. In our study, the reduced intensities of 1 TG and 4 FAs may suggest a decreased demand in energy utilization within the renal tissue after TCC treatment. The reduced levels of various lipid species in LPI, LPE, PA, PE, PG, PC, and PI suggested a significant remodeling of GPs in kidneys treated with TCC. Notably, the disruption of GPs may affect membrane curvature, potentially influencing membrane fission, fusion, and vesicle transport [50]. SM and Cer belonging to sphingolipids (SPs) have been implicated in promoting inflammation in various tissues,

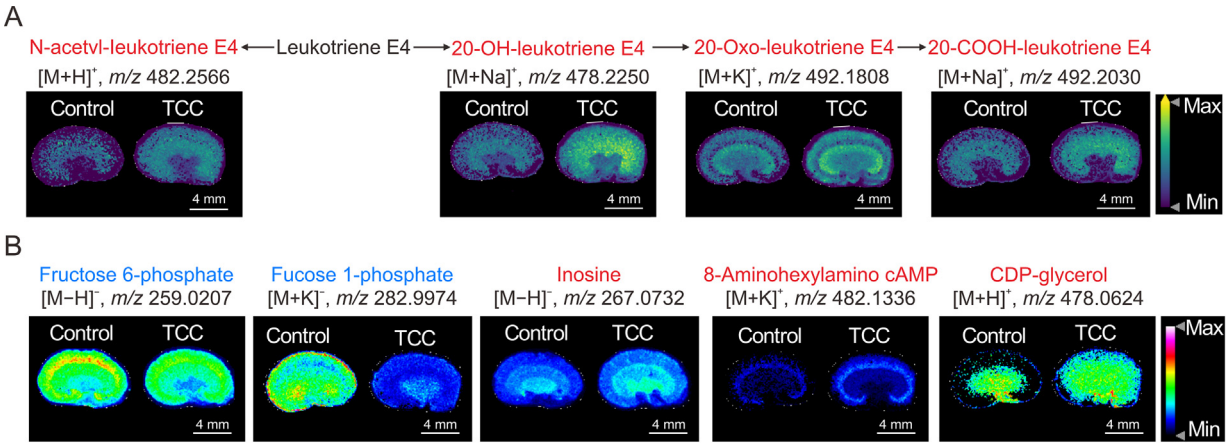

Fig. 5. Ion images of (A) four metabolites involved in leukotriene E4 metabolism and (B) other 5 metabolites in kidney sections between control and TCC groups. The upregulated and downregulated metabolites in kidney sections were represented by red and blue colors, respectively. cAMP: cyclic adenosine monophosphate; CDP: cytidine diphosphate.

including the kidneys [51]. The upregulation of lipid species in Cer and SM in the cortex regions of TCC-treated kidneys may suggest their involvement in inflammatory signaling pathways within the kidney. These disorders of GPs and SPs within the kidneys indicated the effects of TCC on renal cell homeostasis and inflammation, aligning with the data of the histological staining (Fig. 2D). These obtained results were similar to those reported in some previous works [51,52]. Chen et al. [52] demonstrated that the downregulated levels of lipid species in many lipid classes (e.g., PE, PC, PG, PA, and LPE) were found in the injured kidneys treated with perfluorooctane sulfonate (one industrial additive). The upregulated levels of Cer and SM and downregulated levels of PC, PE and PI were linked to the mice nephrotoxicity induced by bisphenol S exposure (one environmental pollutant) [51].

3.5. TCC treatment disturbed the metabolic metabolism in mice kidneys

In addition to lipids, we also detected a total of other 13 and 6 metabolites in positive and negative ionization modes, respectively (Tables S1 and S2). After TCC treatment, the abundances of 9 metabolites in mice kidneys were significantly altered (Tables S1 and S2). These metabolites were involved in several pathways, such as the leukotriene E4 metabolism. In this pathway, three metabolites including *N*-Acetyl-leukotriene E4, 20-OH-leukotriene E4 and 20-Oxo-leukotriene E4 had elevated intensities in all regions of TCC-treated kidney sections, while one metabolite (20-COOH-leukotriene E4) had an increased intensity in three regions (the outer cortex, inner cortex and medulla) of TCC-treated kidney sections (Fig. 5A). Leukotriene E4 is a metabolite derived from the metabolism of arachidonic acid through the action of enzymes like 5-lipoxygenase [53]. It can further undergo different transformations to generate various metabolites, including *N*-acetyl-leukotriene E4, 20-OH-leukotriene E4, 20-Oxo-leukotriene E4, and 20-COOH-leukotriene E4 (Fig. 5A). These metabolites play important roles in inflammation and are involved in the recruitment and activation of inflammatory cells (e.g., eosinophils) and contribute to the development of renal inflammation and tissue damage [54].

For the remaining 5 metabolites, 2 metabolites (fructose 6-phosphate and fucose 1-phosphate) had reduced intensities in all regions, while 3 metabolites including inosine, 8-aminohexylamino cAMP and cytidine diphosphate glycerol (CDP-glycerol) had increased intensities in all regions, three regions (the outer cortex, inner cortex and medulla) and two regions (the outer and inner cortex), respectively (Fig. 5B). Fructose 6-phosphate is primarily generated during glycolysis and plays a crucial role in energy metabolism and biosynthesis [55]. The reduced level of this metabolite may indicate a reduced energy production in kidneys, which was consistent with the reduced levels of FA and TG (Fig. 4B). CDP-glycerol is involved in GPs metabolism and membrane biosynthesis [56]. The changed levels of CDP-glycerol may suggest alterations in membrane lipid composition and cellular signaling in TCC-treated kidneys, which were also consistent with the altered levels of many lipid species in GPs (Fig. 4B).

Fucose 1-phosphate is a phosphorylated form of fucose (a six-carbon sugar) and contributes to the synthesis of glycolipids involved in cell-cell communication and recognition [57]. Inosine is a nucleoside and acts as a precursor for the synthesis of adenosine and guanosine that are important components of RNA and DNA [58]. 8-aminohexylamino cAMP is a derivative of cyclic adenosine monophosphate (cAMP), a critical signaling molecule involved in cellular communication [59]. These alterations of these metabolites may reflect adaptive responses or pathological changes in renal metabolic processes. Further research is still needed to fully understand the specific mechanisms and implications of these metabolic changes after TCC treatment.

Given the physiological congruence between human and rat kidneys, similar metabolic disturbances caused by TCC in mice kidneys may also occur in humans upon exposure. To address these concerns and strengthen public health protection, additional studies including direct examination of TCC effects on human kidney cells and clinical research involving human subjects may also be required. Such studies would help guide the development of appropriate safety guidelines for TCC exposure.

4. Conclusions

In this work, MALDI-MSI-based spatial metabolomics was employed to investigate alterrations of both endogenous and exogenous metabolites in the injured mice kidneys induced by long-term TCC treatment. Our findings demonstrated that TCC localized in all regions of kidneys, while its five metabolites mainly distributed in the cortex regions. A total of 79 metabolites involved in several pathways (e.g., biosynthesis and degradation of GPs and GLs, Cer-SM signaling, and leukotriene E4 metabolism) had significantly changed levels in the kidneys following TCC treatment. The alterations in abundances and spatial distributions of these metabolites could directly reveal nephrotoxic effects of TCC, offering new perspectives on the link between toxicological mechanisms and chemical exposure. The spatial MSI analysis may contribute to a more comprehensive

understanding of the pivotal role of metabolites in TCC-induced nephrotoxicity.

CRediT authorship contribution statement

Peisi Xie: Investigation, Methodology, Validation, Writing – original draft, Data curation, Visualization. **Jing Chen:** Investigation, Data curation, Resources, Writing – review & editing. **Yongjun Xia:** Writing – review & editing. **Zian Lin:** Writing – review & editing. **Yu He:** Writing – review & editing, Funding acquisition. **Zongwei Cai:** Funding acquisition, Supervision, Writing – review & editing.

Declaration of competing interest

As a member of the editorial board of *Journal of Pharmaceutical Analysis*, Zongwei Cai recused himself from the peer review process of this article. The authors declare that there are no conflicts of interest.

Acknowledgments

This work was supported by National Natural Science Foundation of China (Grant Nos.: 22036001 and 22276034).

Appendix A. Supplementary data

Supplementary data to this article can be found online at https://doi.org/10.1016/j.jpha.2024.101024.

References

[1] G. Wang, H. Zhang, J. Zhang, et al., Metabolic fate of environmental chemical triclocarban in colon tissues: Roles of gut microbiota involved, Sci. Total Environ. 787 (2021), 147677.
[2] R.U. Halden, On the need and speed of regulating triclosan and triclocarban in the United States, Environ. Sci. Technol. 48 (2014) 3603–3611.
[3] D. Zhang, S. Lu, A holistic review on triclosan and triclocarban exposure: Epidemiological outcomes, antibiotic resistance, and health risk assessment, Sci. Total Environ. 872 (2023), 162114.
[4] M. Han, Y. Wang, C. Tang, et al., Association of triclosan and triclocarban in urine with obesity risk in Chinese school children, Environ. Int. 157 (2021), 106846.
[5] A.P. Iyer, J. Xue, M. Honda, et al., Urinary levels of triclosan and triclocarban in several Asian countries, Greece and the USA: Association with oxidative stress, Environ. Res. 160 (2018) 91–96.
[6] A. Li, T. Zhuang, Q. Zhu, et al., Concentration and distribution of parabens, triclosan, and triclocarban in pregnant woman serum in China, Sci. Total Environ. 710 (2020), 136390.
[7] D. Iacopetta, A. Catalano, J. Ceramella, et al., The different facets of triclocarban: A review, Molecules 26 (2021), 2811.
[8] X. Xie, C. Lu, M. Wu, et al., Association between triclocarban and triclosan exposures and the risks of type 2 diabetes mellitus and impaired glucose tolerance in the National Health and Nutrition Examination Survey (NHANES 2013-2014), Environ. Int. 136 (2020), 105445.
[9] L.A. Geer, B.F.G. Pycke, J. Waxenbaum, et al., Association of birth outcomes with fetal exposure to parabens, triclosan and triclocarban in an immigrant population in Brooklyn, New York, J. Hazard. Mater. 323 (2017) 177–183.
[10] L. Wei, P. Qiao, Y. Shi, et al., Triclosan/triclocarban levels in maternal and umbilical blood samples and their association with fetal malformation, Clin. Chim. Acta 466 (2017) 133–137.
[11] H.A. Enright, M.J.S. Falso, M.A. Malfatti, et al., Maternal exposure to an environmentally relevant dose of triclocarban results in perinatal exposure and potential alterations in offspring development in the mouse model, PLoS One 12 (2017), e0181996.
[12] R.C. Kennedy, R.R. Fling, M.S. Robeson, et al., Temporal development of gut microbiota in triclocarban exposed pregnant and neonatal rats, Sci. Rep. 6 (2016), 33430.
[13] A. Hinther, C.M. Bromba, J.E. Wulff, et al., Effects of triclocarban, triclosan, and methyl triclosan on thyroid hormone action and stress in frog and mammalian culture systems, Environ. Sci. Technol. 45 (2011) 5395–5402.
[14] Y. Wu, F.A. Beland, J. Fang, Effect of triclosan, triclocarban, 2,2′,4,4′-tetrabromodiphenyl ether, and bisphenol A on the iodide uptake, thyroid peroxidase activity, and expression of genes involved in thyroid hormone synthesis, Toxicol. In Vitro 32 (2016) 310–319.
[15] H. Zhang, Y. Liang, P. Wu, et al., Continuous dermal exposure to triclocarban perturbs the homeostasis of liver-gut axis in mice: Insights from metabolic interactions and microbiome shifts, Environ. Sci. Technol. 55 (2021) 5117–5127.
[16] H. Yang, K.Z. Sanidad, W. Wang, et al., Triclocarban exposure exaggerates colitis and colon tumorigenesis: Roles of gut microbiota involved, Gut Microbes 12 (2020), 1690364.
[17] H. Zhang, Y. Lu, Y. Liang, et al., Triclocarban-induced responses of endogenous and xenobiotic metabolism in human hepatic cells: Toxicity assessment based on nontargeted metabolomics approach, J. Hazard. Mater. 392 (2020), 122475.
[18] X. Li, J.-D. Zhang, H. Xiao, et al., Triclocarban and triclosan exacerbate high-fat diet-induced hepatic lipid accumulation at environmental related levels: The potential roles of estrogen-related receptors pathways, Sci. Total Environ. 858 (2023), 160079.
[19] Y. Zhou, X. Jiang, X. Wang, et al., Promise of spatially resolved omics for tumor research, J. Pharm. Anal. 13 (2023) 851–861.
[20] X.-W. Zhang, Q.-H. Li, Z. Xu, et al., Mass spectrometry-based metabolomics in health and medical science: A systematic review, RSC Adv. 10 (2020) 3092–3104.
[21] Q. Dai, P. Xie, H. Tan, et al., Metabolomics and lipidomics with mass spectrometry imaging reveal mechanistic insights into dibutyl phthalate-promoted proliferation of breast cancer cell spheroids, Environ. Sci. Technol. Lett. 11 (2024) 208–215.
[22] T. Liu, R. Li, Y. Cui, et al., Metabonomic analysis of plasma biochemical changes in pyrexia rats after treatment with Gegenqinlian decoction, aspirin and itraconazole by UHPLC-FT-ICR-MS, J. Pharm. Anal. 10 (2020) 581–587.
[23] W. Xie, W. Zhang, J. Ren, et al., Metabonomics indicates inhibition of fatty acid synthesis, β-oxidation, and tricarboxylic acid cycle in triclocarban-induced cardiac metabolic alterations in male mice, J. Agric. Food Chem. 66 (2018) 1533–1542.
[24] Y. Liu, X. Zhang, S. Yang, et al., Integrated mass spectrometry imaging reveals spatial-metabolic alteration in diabetic cardiomyopathy and the intervention effects of ferulic acid, J. Pharm. Anal. 13 (2023) 1496–1509.
[25] C. Sun, L. Cui, B. Zhou, et al., Visualizing the spatial distribution and alteration of metabolites in continuously cropped Salvia miltiorrhiza Bge using MALDI-MSI, J. Pharm. Anal. 12 (2022) 719–724.
[26] P. Xie, J. Chen, P. Wu, et al., Spatial lipidomics reveals lipid changes in the cotyledon and plumule of mung bean seeds during germination, J. Agric. Food Chem. 71 (2023) 19879–19887.
[27] P.E. Feist, S. Sidoli, X. Liu, et al., Multicellular tumor spheroids combined with mass spectrometric histone analysis to evaluate epigenetic drugs, Anal. Chem. 89 (2017) 2773–2781.
[28] G.J. LaBonia, K.R. Ludwig, C.B. Mousseau, et al., iTRAQ quantitative proteomic profiling and MALDI-MSI of colon cancer spheroids treated with combination chemotherapies in a 3D printed fluidic device, Anal. Chem. 90 (2018) 1423–1430.
[29] Z. Wang, B. He, Y. Liu, et al., In situ metabolomics in nephrotoxicity of aristolochic acids based on air flow-assisted desorption electrospray ionization mass spectrometry imaging, Acta Pharm. Sin. B 10 (2020) 1083–1093.
[30] Y. Chen, T. Wang, P. Xie, et al., Mass spectrometry imaging revealed alterations of lipid metabolites in multicellular tumor spheroids in response to hydroxychloroquine, Anal. Chim. Acta 1184 (2021), 339011.
[31] S. Kim, K. Koppitch, R.K. Parvez, et al., Comparative single-cell analyses identify shared and divergent features of human and mouse kidney development, Dev. Cell 21 (2024) 2912–2930.
[32] J. Schnell, M. Achieng, N.O. Lindström, Principles of human and mouse nephron development, Nat. Rev. Nephrol. 18 (2022) 628–642.
[33] X. Ye, L.Y. Wong, P. Dwivedi, et al., Urinary concentrations of the antibacterial agent triclocarban in United States residents: 2013-2014 national health and nutrition examination survey, Environ. Sci. Technol. 50 (2016) 13548–13554.
[34] R.A. Hiles, C.G. Birch, The absorption, excretion, and biotransformation of 3,4,4′-trichlorocarbanilide in humans, Drug Metab. Dispos. 6 (1978) 177–183.
[35] C. Rose, A. Parker, B. Jefferson, et al., The characterization of feces and urine: A review of the literature to inform advanced treatment technology, Crit. Rev. Environ. Sci. Technol. 45 (2015) 1827–1879.
[36] W. Li, W. Zhang, M. Chang, et al., Metabonomics reveals that triclocarban affects liver metabolism by affecting glucose metabolism, β-oxidation of fatty acids, and the TCA cycle in male mice, Toxicol. Lett. 299 (2018) 76–85.
[37] M. Dong, X. Xu, Q. Huang, et al., Dose-dependent effects of triclocarban exposure on lipid homeostasis in rats, Chem. Res. Toxicol. 32 (2019) 2320–2328.
[38] E. Fröhlich, Animals in respiratory research, Int. J. Mol. Sci. 25 (2024), 2903.
[39] P. Xie, H. Zhang, P. Wu, et al., Three-dimensional mass spectrometry imaging reveals distributions of lipids and the drug metabolite associated with the enhanced growth of colon cancer cell spheroids treated with triclosan, Anal. Chem. 94 (2022) 13667–13675.
[40] J. Chen, P. Xie, P. Wu, et al., Spatial metabolomics and lipidomics reveal the mechanisms of the enhanced growth of breast cancer cell spheroids exposed to triclosan, Environ. Sci. Technol. 57 (2023) 10542–10553.
[41] N.H. Schebb, J.B. Muvvala, D. Morin, et al., Metabolic activation of the antibacterial agent triclocarban by cytochrome P450 1A1 yielding glutathione adducts, Drug Metab. Dispos. 42 (2014) 1098–1102.
[42] N.H. Schebb, I. Flores, T. Kurobe, et al., Bioconcentration, metabolism and excretion of triclocarban in larval Qurt medaka (Oryzias latipes), Aquat. Toxicol. 105 (2011) 448–454.

[43] P. David Josephy, F. Peter Guengerich, J.O. Miners, "Phase I and Phase II" drug metabolism: Terminology that we should phase out? Drug Metab. Rev. 37 (2005) 575–580.
[44] Z. Shen, C. Lv, S. Zeng, Significance and challenges of stereoselectivity assessing methods in drug metabolism, J. Pharm. Anal. 6 (2016) 1–10.
[45] H. Zhang, X. Shao, H. Zhao, et al., Integration of metabolomics and lipidomics reveals metabolic mechanisms of triclosan-induced toxicity in human hepatocytes, Environ. Sci. Technol. 53 (2019) 5406–5415.
[46] N.H. Schebb, B. Inceoglu, K.C. Ahn, et al., Investigation of human exposure to triclocarban after showering and preliminary evaluation of its biological effects, Environ. Sci. Technol. 45 (2011) 3109–3115.
[47] D.J. Watkins, K.K. Ferguson, L.V. Anzalota Del Toro, et al., Associations between urinary phenol and paraben concentrations and markers of oxidative stress and inflammation among pregnant women in Puerto Rico, Int. J. Hyg. Environ. Health 218 (2015) 212–219.
[48] J. Wei, T. Zhou, Z. Hu, et al., Effects of triclocarban on oxidative stress and innate immune response in zebrafish embryos, Chemosphere 210 (2018) 93–101.
[49] M. Alves-Bezerra, D.E. Cohen, Triglyceride metabolism in the liver, Compr. Physiol. 8 (2017) 1–8.
[50] M. Pinot, S. Vanni, S. Pagnotta, et al., Polyunsaturated phospholipids facilitate membrane deformation and fission by endocytic proteins, Science 345 (2014) 693–697.
[51] C. Zhao, P. Xie, T. Yong, et al., MALDI-MS imaging reveals asymmetric spatial distribution of lipid metabolites from bisphenol S-induced nephrotoxicity, Anal. Chem. 90 (2018) 3196–3204.
[52] Y. Chen, L. Jiang, R. Zhang, et al., Spatially revealed perfluorooctane sulfonate-induced nephrotoxicity in mouse kidney using atmospheric pressure MALDI mass spectrometry imaging, Sci. Total Environ. 838 (2022), 156380.
[53] H.R. Foster, E. Fuerst, W. Branchett, et al., Leukotriene E4 is a full functional agonist for human cysteinyl leukotriene type 1 receptor-dependent gene expression, Sci. Rep. 6 (2016), 20461.
[54] E. Duah, R.K. Adapala, N. Al-Azzam, et al., Cysteinyl leukotrienes regulate endothelial cell inflammatory and proliferative signals through $CysLT_2$ and $CysLT_1$ receptors, Sci. Rep. 3 (2013), 3274.
[55] F. Rajas, A. Gautier-Stein, G. Mithieux, Glucose-6 phosphate, a central hub for liver carbohydrate metabolism, Metabolites 9 (2019), 282.
[56] M.V. Rodrigues, N. Borges, H. Santos, Glycerol phosphate cytidylyltransferase stereospecificity is key to understanding the distinct stereochemical compositions of glycerophosphoinositol in Bacteria and Archaea, Appl. Environ. Microbiol. 83 (2016) e02462–16.
[57] J. Li, H.C. Hsu, J.D. Mountz, et al., Unmasking fucosylation: From cell adhesion to immune system regulation and diseases, Cell Chem. Biol. 25 (2018) 499–512.
[58] F.P. Nascimento, S.J. Macedo-Júnior, F.R. Lapa-Costa, et al., Inosine as a tool to understand and treat central nervous system disorders: A neglected actor? Front. Neurosci. 15 (2021), 703783.
[59] S. Delhaye, B. Bardoni, Role of phosphodiesterases in the pathophysiology of neurodevelopmental disorders, Mol. Psychiatry 26 (2021) 4570–4582.